

ON THE ORIGIN OF MID-LATITUDE FAST WIND: CHALLENGING  
THE TWO-STATE SOLAR WIND PARADIGMMARK STAKHIV<sup>1</sup>, ENRICO LANDI<sup>2</sup>, SUSAN T. LEPRI<sup>3</sup>, RONA ORAN<sup>4,5</sup>, AND THOMAS H. ZURBUCHEN<sup>6</sup>Department of Atmospheric, Oceanic, and Space Sciences, University of Michigan, Ann Arbor, MI 48109-2143, USA;  
[mstakhiv@umich.edu](mailto:mstakhiv@umich.edu), [elandi@umich.edu](mailto:elandi@umich.edu), [slepri@umich.edu](mailto:slepri@umich.edu), [oran@umich.edu](mailto:oran@umich.edu), [ronan@mit.edu](mailto:ronan@mit.edu), [thomasz@umich.edu](mailto:thomasz@umich.edu)

Received 2014 August 22; accepted 2015 January 11; published 2015 March 11

## ABSTRACT

The bimodal paradigm of solar wind describes a slow solar wind situated near the heliospheric current sheet while a fast wind overexpands from the poles to fill in the remainder of the heliosphere. In this paper, we challenge this paradigm and focus here on mid-latitude wind using three fast-latitude passes completed by the *Ulysses* spacecraft. Based on its composition and dynamic properties, we discuss how this wind differs from both the fast, polar coronal hole wind and the low latitude, streamer-associated slow solar wind. Using a detailed analysis of ionic and elemental abundances, as well as solar wind dynamic properties, we conclude that there is a third quasi-stationary solar wind state, called the boundary wind. This boundary wind is characterized by a charge-state distribution that is similar to slow wind, but with an elemental composition that is coronal hole like. Based on these data, we present arguments for the location of the origin of this wind. We conclude that the boundary wind is a subset of the fast wind emanating from regions close to the boundaries of coronal holes and is accelerated by a similar process.

*Key words:* solar wind – Sun: abundances – Sun: corona – Sun: heliosphere

## 1. INTRODUCTION

The solar wind observed in the heliosphere has traditionally been categorized into two quasi-stationary types based on its composition (e.g., Zurbuchen 2007 and references therein): fast, coronal-hole-associated wind and slow solar wind associated with streamers. This two-state phenomenon is most obvious in its observed wind composition, which reflects both its origin as well as the wind's expansion history. Results from the *Ulysses* mission revealed that there was an inverse correlation between the charge-state ratios (i.e.,  $O^{7+}/O^{6+}$ ) and solar wind speed (Geiss et al. 1995; Gloeckler et al. 2003). The solar wind charge states are determined by the electron temperature, density, and plasma flow velocity in the expanding corona before the freeze-in point (typically  $<3-5 R_s$ ) after which the ionic composition remains unchanged. The elevated charge states of oxygen in the slow solar wind indicate that there is an increase of electron temperature and/or density coupled with a relatively low velocity in the regions where it originates, allowing the ionic charge states to adapt more efficiently to the high temperatures of the inner corona. In contrast, the fast wind, associated with coronal holes, reflects an origin with lower electron temperature and density. A second characteristic difference between fast and slow solar wind is the elemental composition. Using mid- and high-latitude solar wind data measured onboard *Ulysses*, Geiss et al. (1995) found that the elemental composition of the wind is rather bimodal. The fast wind composition is approximately

photospheric, while the slow wind is enhanced in elements with low first ionization potential (FIP), similar to the composition of the closed corona. A third characteristic distinguishing the solar wind types is the variability in both dynamic and compositional properties (Gosling 1997). The fast wind tends to have rather constant compositional signatures while the slow wind is more variable in nature (Zurbuchen & von Steiger 2006).

This bimodal picture of the solar wind has also been described using other heliospheric data sets, especially in the inner heliosphere where the solar wind is more dynamically pristine and has yet to have its sharp transitions eroded due to momentum transfer between the fast and slow solar wind. For example, Schwenn (1990) summarizes Helios data and suggests that there is a very sharp transition between a fast, rather steady solar wind and a slow, variable wind near the heliospheric current sheet. That nearly abrupt transition becomes increasingly evident the closer Helios observed near the Sun. Similarly, the inner state of the solar wind reflects this bimodal state. Fast wind velocity distribution functions exhibit distinctive deviations from a thermal equilibrium whereas slow wind streams are more Maxwellian (Marsch et al. 1982b; Marsch 1991). Also, the turbulence exhibited in fast solar wind streams is indicative of outward propagating Alfvén waves, whereas slow winds exhibit a more bi-directional turbulent spectrum (Marsch 1991).

The physical processes that heat the open corona and the solar wind are still an ongoing topic of research. Several models and theories have been put forth to explain how the solar wind is heated and accelerated, which also link the acceleration process to the specific location of the source region of the wind. One such theory suggests that the solar wind is heated by wave dissipation and accelerated by gradients in the Alfvén wave pressure (e.g., Belcher & Davis 1971; Hollweg 1986; Cranmer et al. 2007; van der Holst et al. 2014 and references therein). These theoretical models predict that the turbulent motions at the photosphere and chromosphere give rise to significant amounts of Alfvén waves and that the energy in these waves can be tapped through a variety of processes to accelerate the solar wind. Another model put forth by Lemaire & Scherer (1971) suggests that the ions are accelerated by a charge separation

<sup>1</sup> PhD candidate in Space Science, 2134A Space Research Building, 2455 Hayward Street, Ann Arbor, MI 48109-2143, USA.

<sup>2</sup> Research Scientist, 2426 Space Research Building, 2455 Hayward Street, Ann Arbor, MI 48109-2143, USA.

<sup>3</sup> Associate Professor, 2429 Space Research Building, 2455 Hayward Street, Ann Arbor, MI 48109-2143, USA.

<sup>4</sup> PhD, 2455 Hayward Street, Ann Arbor, MI 48109-2143, USA.

<sup>5</sup> Post-doctoral Associate, Department of Earth, Atmospheric and Planetary Sciences, Massachusetts Institute of Technology, Cambridge, MA 02139, USA.

<sup>6</sup> Professor, Space Science and Aerospace Engineering, Associate Dean for Entrepreneurship Senior Counselor of Entrepreneurship Education, 2431 Space Research Building, 2455 Hayward Street, Ann Arbor, MI 48109-2143, USA.

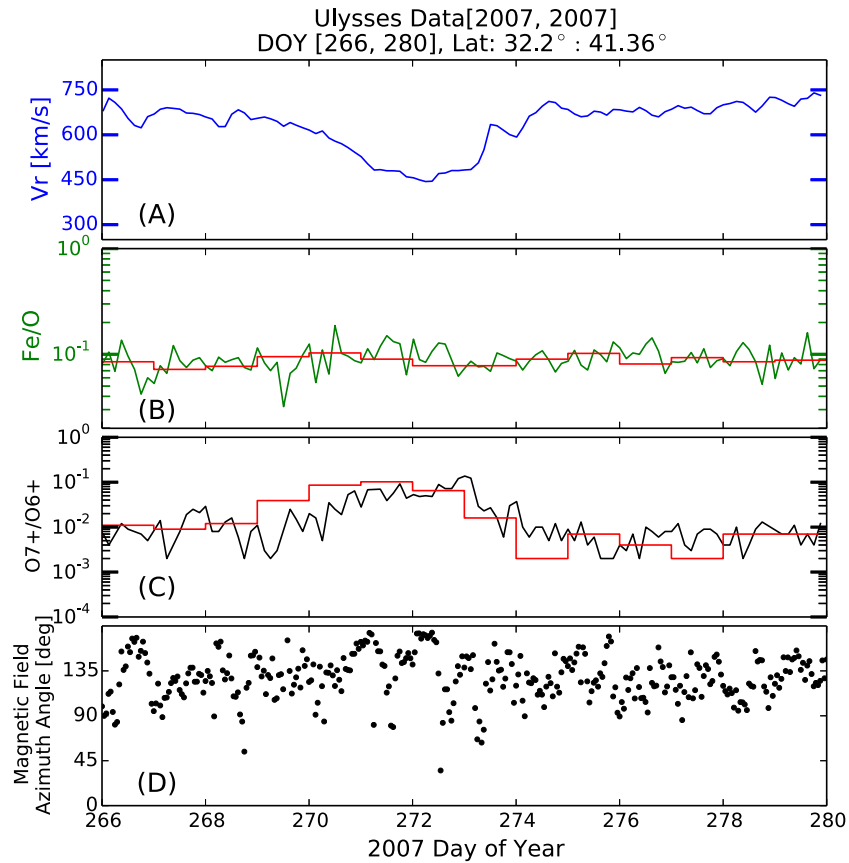


**Figure 1.** Fourteen day plot of solar wind using velocity and compositional data. Panel (A) shows the proton velocity that shows a decrease from coronal hole values to a speed intermediate between slow and coronal hole wind. Panel (D) shows the azimuthal angle of the wind’s magnetic field and indicates that the current sheet was not crossed. Panel (B) shows the wind’s Fe/O ratio in 3 hr intervals (green) and 24 hr intervals (red). Panel (C) shows  $O^{7+}/O^{6+}$  ratios in 3 hr intervals (black) and 24 hr intervals (red). The transition to slower wind is accompanied by an increase of the  $O^{7+}/O^{6+}$  ratio to values typical of streamer-associated slow wind. The elemental composition does not change.

electric field. This electric field is set up by a larger escape flux of electrons than protons caused by the difference in their thermal velocities (Lemaire & Scherer 1973; Parker 2010). In both of these theories the acceleration occurs along open field lines associated with coronal holes.

Another method of acceleration that has been proposed is magnetic reconnection (e.g., Fisk 2003, or Crooker et al. 2002). These theories predict that the interchange reconnection between open and closed magnetic field lines can accelerate plasma previously captured on magnetic loops into the heliosphere, consistent with the compositional signatures of slow wind. Most recently, Antiochos et al. (2011) introduced the S-Web model, suggesting that magnetic reconnection along highly complex coronal holes boundaries is a source of the slow solar wind.

However, none of the proposed scenarios is able to account for all the properties of both types of the wind: acceleration and heating due to Alfvén waves may be steady, so by itself it cannot reproduce the patchiness and variability of the slow wind; wind acceleration along steady open field lines can only come from coronal holes, and thus should have near photospheric abundances, so it cannot account for the reported coronal element composition of the slow wind, which is typical of closed magnetic loops in the corona (e.g., Feldman et al. 2005). It is possible that multiple acceleration and heating theories are correct and that the fast and slow solar wind are heated and accelerated due to different processes, resulting in different signatures in the solar wind.

The simple bimodal picture that the solar wind is made up of either fast or slow wind is not always accurate, especially near solar activity maximum. The limitation in classifying the wind into either fast or slow streams has previously been investigated by Zurbuchen et al. (2002), which reported that during solar minimum the velocity and  $O^{7+}/O^{6+}$  ratio appear bimodal, whereas during solar maximum this bimodal nature is replaced by a single peaked distribution covering a broader range of coronal temperatures and densities. Despite the continuum of dynamic states the elemental composition remains rather bimodal, with the lowest charge-state wind having near-photospheric composition and the higher charge-state wind exhibiting fractionated, coronal composition. Figure 1 shows a 14 day interval of *Ulysses* solar wind data gathered between  $32^\circ$  and  $42^\circ$  latitude in 2007 that challenges the bimodal nature of the wind. This figure shows an observed transition from fast wind to slower wind and then another transition back to fast wind. Characteristics of these transitions can be seen in both the velocity (panel (A)) and the oxygen charge states (panel (C)). Panel (D) further shows that these fast–slow and slow–fast transitions occur in one and the same magnetic sector, without a transition through the heliospheric current sheet. The elemental composition (panel (B)), surprisingly, does not exhibit any transitions but stays rather constant, consistent with coronal-hole-associated wind. Most importantly, the wind that *Ulysses* observed between days 270 and 273 had elemental composition identical to the fast solar wind but had ion charge states and velocity that were typical of the slow solar wind. The aim of this paper is to perform an

analysis of solar wind data during the three fast-latitude passes performed by *Ulysses* in order to analyze when and why cases such as in Figure 1 occur. We will place emphasis on looking for slow velocity solar wind that has photospheric abundances and comparing its composition and kinetic properties to the purely fast and slow solar wind.

We will first introduce the data used in this study in Section 2, and then analyze the mid-latitude wind in Section 3 focused on three fast-latitude passes by *Ulysses*, measurements taken near the periapsis passes of this mission. Section 4 will discuss the finding of this new type of solar wind and its implications in the overall picture of the solar wind.

## 2. OBSERVATIONS

Data used for this analysis were obtained from three different instruments providing measurements of solar wind composition, plasma characteristics and magnetic field. Compositional data from Solar Wind Ion Composition Spectrometer (SWICS) were taken from the *Ulysses* archive and have 3 hr time resolution. Sometimes, 24 hr time resolution data were also used, especially to separate statistical variability from real compositional changes. The  $\text{Fe}/\text{O}$ ,  $\text{C}^{6+}/\text{C}^{5+}$ ,  $\text{O}^{7+}/\text{O}^{6+}$ ,  $\text{He}^{2+}$  velocity,  $\text{O}^{6+}$  kinetic temperature, and  $\text{O}^{6+}$  velocity data products from the SWICS instrument were used in this analysis. For more details about the analysis procedure and the instrument refer to Gloeckler et al. (1992) and von Steiger et al. (2000). We used proton velocity, temperature, and density plasma data measured from the Solar Wind Observations Over the Poles of the Sun (Bame et al. 1992). Finally, we used 1 hr magnetic field measurements from the Vector Helium Magnetometer (Balogh et al. 1992). All three data sets are available at the *Ulysses* archive at <http://ufa.esac.esa.int/>. This combination of data is uniquely suitable for this analysis for two principal reasons. First, the length of the *Ulysses* data set extends nearly 20 yr covering almost a full magnetic cycle of the Sun. This length of time allows us to study the solar wind over the course of multiple solar minima. Second, the *Ulysses* spacecraft had a unique polar orbit that allowed for measurements away from the ecliptic plane, unlike the in-ecliptic measurements available from other instruments. This polar orbit allows analyzing the solar wind at all latitudes.

This paper focused on three periapsis passes of *Ulysses*, the so-called “fast-latitude scans” that *Ulysses* performed during each polar pass. The three fast-latitude scans occurred approximately 6 yr apart and consisted of a nearly full  $180^\circ$  latitude scan. These passes transverse the full range of latitudes in about a year, covering both the poles and the ecliptic plane and allowing us to study all types of solar wind on three different occasions: two of the passes occurred during solar minimum (centered around the years 1995 and 2007) separated by a pass which took place during solar maximum (centered around 2001), allowing us to see the changes in the solar wind during maximum and minimum and from solar cycle to solar cycle. To the best of our ability, time periods of interplanetary coronal mass ejections (ICMEs) have been filtered out of the data due to their well-documented anomalies and transient nature. The ICME list provided by Ebert et al. (2009) was used to eliminate ICME-associated data from this analysis.

## 3. RESULTS

Figure 2 shows a scatter plot of the elemental composition and charge-state data for pass 1 (1995), plotted against the proton

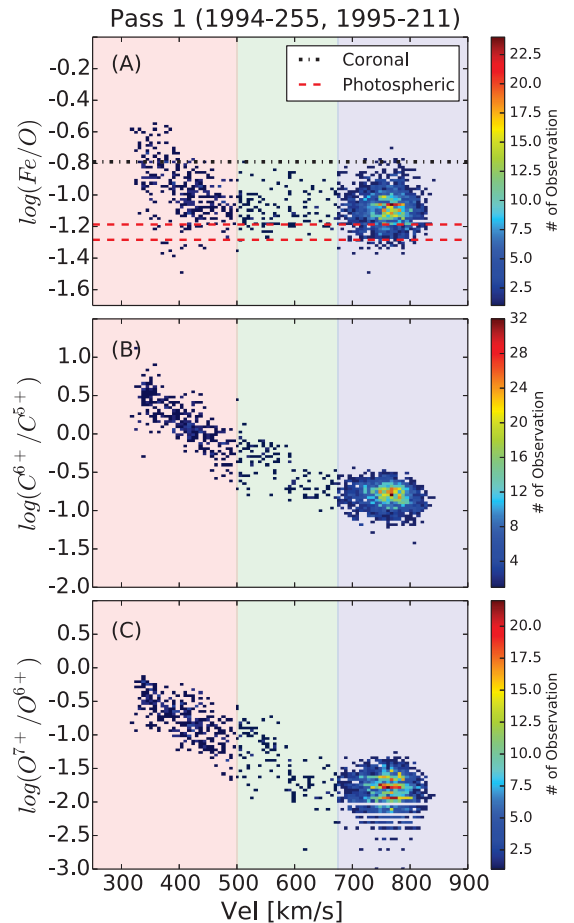


**Figure 2.** Compositional properties during the first *Ulysses* fast-latitude scan. This pass occurred around the 1996 solar minimum. The highlighted colors in the background of the plots indicate the different types of solar wind: slow (red), boundary (green), and fast (blue). Panel (A) shows the winds  $\text{Fe}/\text{O}$  ratio. In this panel the red dotted lines indicates the measured photospheric values for this ratio and the black dotted line shows the observed coronal value. Panel (B) shows the  $\text{C}^{6+}/\text{C}^{5+}$  ratio and panel (C) shows the  $\text{O}^{7+}/\text{O}^{6+}$  ratio (the horizontal strips in the ratio are a data artifact caused by the number of significant digits reported and the logarithmic spacing of the histogram). As the velocity of the solar wind increases the charge-state ratio decreases exponentially. The compositional ratio ( $\text{Fe}/\text{O}$ ) only shows a divide in its behavior with respect to the proton speed at  $500 \text{ km s}^{-1}$ .

speed. In this figure we show the  $\text{Fe}/\text{O}$  ratio (panel (A)), carbon charge-state ratio ( $\text{C}^{6+}/\text{C}^{5+}$ ) (panel (B)), and oxygen charge-state ratio ( $\text{O}^{7+}/\text{O}^{6+}$ ) (panel (C)). Panels (B) and (C) show the charge-state ratios measured by *Ulysses* as a function of speed, which demonstrate that as the solar wind speed increases, the charge states decrease, creating a strong anti-correlation. In this figure we see that *Ulysses* mostly observed the fast solar wind ( $\sim 750 \text{ km s}^{-1}$ ) during this period due to the fact that it spends more time at higher latitudes. This solar wind has an average  $\text{C}^{6+}/\text{C}^{5+}$  ratio of around 0.177. There is an exponential relationship between the charge-state ratios and the speed of the solar wind (as previously reported by Geiss et al. 1995). Panel (A) tells a different story. In this panel the  $\text{Fe}/\text{O}$  ratio is used as a proxy for the element fractionation in solar wind plasma because it is the abundance ratio between an element with FIP smaller than 10 eV, iron, and one with FIP greater than 10 eV, oxygen. The ratio between a low-FIP to a high-FIP element is a tracer of the FIP effect, namely the still not understood enhancement of the abundance ratio of low-FIP to high-FIP elements in the solar corona over the

same ratio in the photosphere (e.g., Feldman & Laming 2000, and references therein). The degree of enhancement in the coronal low-FIP/high-FIP abundance ratio is called the “FIP bias” and typically ranges from 1, in the coronal holes, to 3–4 in closed field regions. These abundance anomalies are directly propagated into the solar wind plasma emanating from the corona, so that the ratio in panel (A) gives an indication of the source region of the wind itself. In panel (A) the reported photospheric values ( $\log(\text{Fe}/\text{O}) = -1.33$ , Grevesse & Sauval 1998;  $\log(\text{Fe}/\text{O}) = -1.16$ , Asplund et al. 2009) are marked with dotted red lines, along with the reported coronal value ( $\log(\text{Fe}/\text{O}) = -0.74$ —Feldman 1992) marked with a dotted black line. The value of the photospheric abundance ratio is marked by two lines to highlight the range of Fe/O ratio due to the uncertainties in the photospheric abundance of oxygen. We can see in these panels that the fast solar wind has elemental abundances just above photospheric values and that there is no correlation between Fe/O and velocity, as there was with  $\text{O}^{7+}/\text{O}^{6+}$  and  $\text{C}^{6+}/\text{C}^{5+}$ . As the velocity decreases from the fast solar wind value of approximately  $750 \text{ km s}^{-1}$ , the Fe/O ratio remains at near photospheric values until around  $500 \text{ km s}^{-1}$ . At this point the Fe/O ratio starts to increase to higher values. It is interesting to note that this is not a systematic increase as is seen in the ion charge states of oxygen and carbon. Although the mean Fe/O ratio does increase for speeds below  $500 \text{ km s}^{-1}$  there are still values with near photospheric abundances even at the lowest speeds. If we interpret the Fe/O ratio alone as a tracer of the source region, panel (A) shows that the wind with speeds greater than  $500 \text{ km s}^{-1}$  comes from the same source region even if its charge-state ratios change systematically. On the contrary, the coexistence of Fe/O ratios spanning a factor of three in the wind with velocity less than  $500 \text{ km s}^{-1}$  indicates that this wind could come from multiple source regions that may include the same source region as the fast wind, as well as a multitude of other different sources with FIP bias ranging from one to around three. The variability of the FIP bias in wind streams slower than  $500 \text{ km s}^{-1}$  could be due to the portion of this wind with Fe/O ratio larger than fast wind value coming from plasma initially confined in closed magnetic loops in the corona, which are opened up by reconnection (e.g., Fisk 2003; Antiochos et al. 2011). This scenario is supported by two facts.

1. The FIP bias in the wind slower than  $500 \text{ km s}^{-1}$  is consistent with values routinely reported in spectroscopic measurements (Feldman & Laming 2000; Feldman et al. 2005).
2. The variability of this FIP bias is consistent with variability of this parameter in the corona, which has been suggested to be due to the varying age of coronal loops (Widing & Feldman 2001).

The wind streams with intermediate speeds between the fast and slow wind seen in this figure ( $500\text{--}675 \text{ km s}^{-1}$ , highlighted in green) cannot be characterized with the standard signatures as either fast or slow solar wind since they have a combination of the characteristics of both wind types. This wind has intermediate values of both velocity and charge states, slower and more ionized than fast solar wind, but has elemental composition similar to the fast wind. This indicates that this wind likely originates from the same plasma as the fast solar wind, but undergoes less acceleration, as well as more ionization leading to an increase in the charge-state ratios. In this section we argue that this wind is a subset of the fast wind that originates from

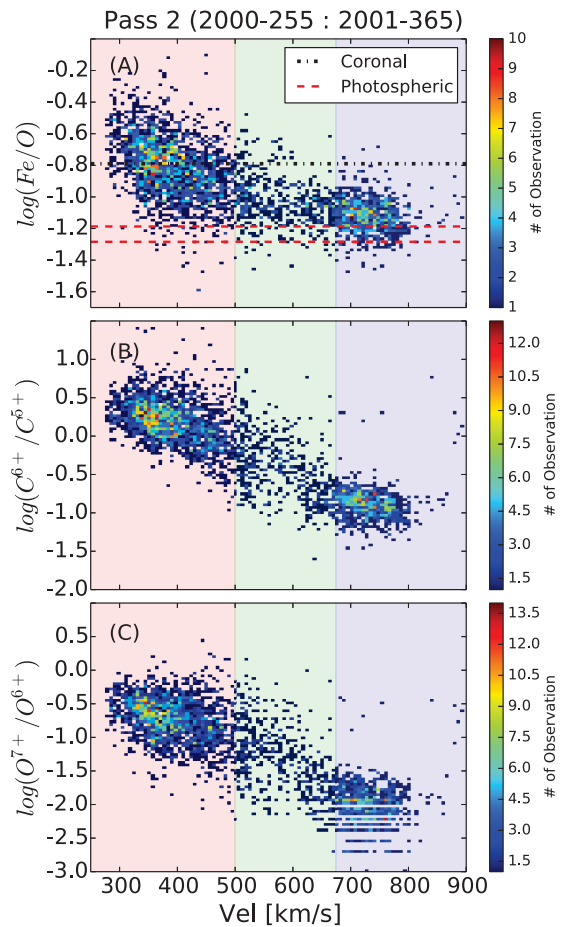


**Figure 3.** Compositional properties during the second Ulysses fast-latitude scan. This figure is the same as Figure 2, but occurring 6 yr later during the 2001 solar maximum. The same trends seen in Figure 2 are seen here.

inside coronal holes, yet near the boundary, leading us to name it the boundary wind.

Figure 3 has identical panels as Figure 2 but is measured 6 yr later during solar maximum. Here the statistics in the slow wind are enhanced because the slow wind is found at a much larger range of latitudes due to increased inclination and warping of the current sheet during solar maximum. In this figure we can see the same trends that were pointed out in Figure 2. Both of the charge-state ratios (panels (B) and (C)) show an exponential dependence on speed, while the elemental compositional parameter (panel (A)) shows near photospheric values for speeds above  $500 \text{ km s}^{-1}$ . Figure 4 is again similar to Figures 2 and 3 but is measured 6 yr later during the next solar minimum. This figure also shows the same trends as Figures 2 and 3, indicating that the main compositional properties of the solar wind and their dependence on wind speed do not change along the solar cycle.

From the results shown in panel (A) of Figures 2–4 we argue that the distribution of the Fe/O ratio for the wind between  $500 \text{ km s}^{-1}$  and  $675 \text{ km s}^{-1}$  is similar to that found in wind streams faster than  $675 \text{ km s}^{-1}$ . Figure 5 shows the distribution for Fe/O ratio for pass 2 (corresponding to panel (A) in Figure 3). This figure separates the data into three panels: the slow wind (panel (A)) corresponding to the Fe/O ratio below  $500 \text{ km s}^{-1}$  (red highlighted area in Figure 3), the fast wind (panel (B)) corresponding to the Fe/O ratio above  $675 \text{ km s}^{-1}$  (blue highlighted area in Figure 3), and the boundary wind (panel (C)) corresponding to the Fe/O ratio



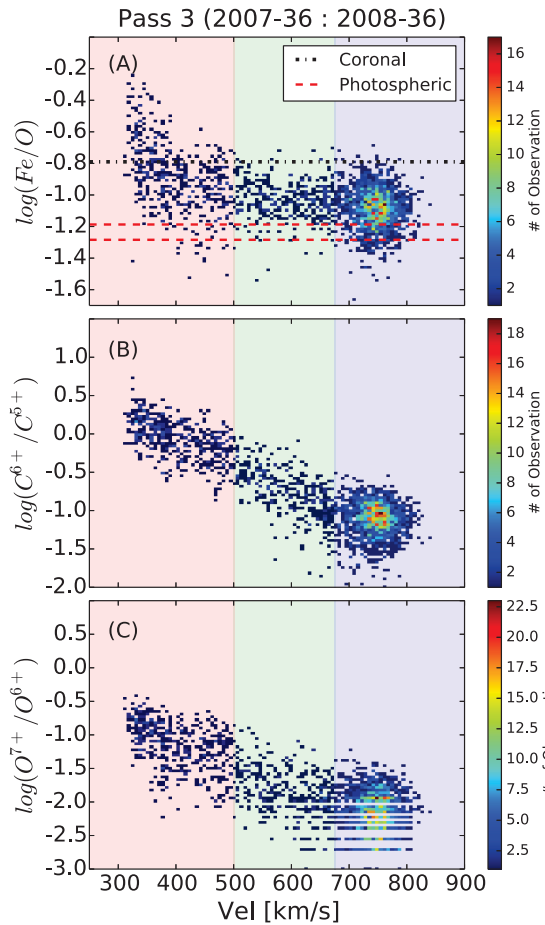


**Figure 4.** Compositional properties during the third Ulysses fast-latitude scan. This figure is the same as Figure 2 but occurring 12 yr later during the 2007 solar minimum. The same trends seen in Figure 2 are seen here, indicating that the properties seen in the figure are not solar cycle dependent.

between  $500 \text{ km s}^{-1}$  and  $675 \text{ km s}^{-1}$  (green highlighted area in Figure 3). The curves on these three panels (red) are Gaussian fits of the data. The red line indicates the mean in log space and the error bar shows one standard deviation from the mean in log space. In this figure we can see that the distribution of the data in panels (B) and (C) are very similar to each other and distinctly different than that of panel (A). Although the mean of panels (B) and (C) are not identical this is not unexpected. Panel (C) has a slight tail at higher Fe/O ratio most likely caused by capturing some slow solar wind values in the  $500\text{--}675 \text{ km s}^{-1}$  range. This speaks to the nature of this lower boundary (at  $500 \text{ km s}^{-1}$ ) being highly dynamic. Without this variability of this boundary, the mean would shift even closer to the fast solar wind value seen in panel (B).

The kinetic properties of the solar wind provide a wealth of information along with the element compositional properties. In order to further solidify the similarities between the boundary wind and the fast wind, the differential velocity, temperature ratio, and entropy of the passes were analyzed. All three of the fast-latitude scan passes were summed to generate Figure 6. This was done to allow for sufficient statistics for both the fast and slow wind. In these panels the data has been filtered to only include intervals with nearly radial magnetic field, as differential velocity is most accurately estimated in this configuration (for details, refer to von Steiger & Zurbuchen 2006). We require intervals to have a magnetic field persistent within  $30^\circ$  of radial for over 66% of the time. Panels (A) and (C) show

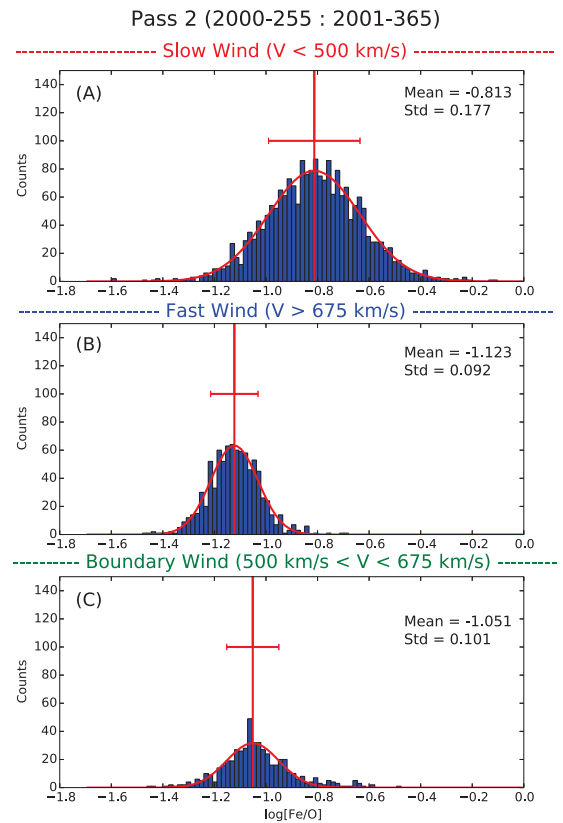


**Figure 5.** Distribution of Fe/O ratio for the second pass: 2000-255–2001-365. Panel (A) shows the Fe/O ratio for all values slower than  $500 \text{ km s}^{-1}$ . Panel (B) shows the Fe/O ratio for all values faster than  $675 \text{ km s}^{-1}$ . Panel (C) shows the Fe/O ratio for all values between  $500 \text{ km s}^{-1}$  and  $675 \text{ km s}^{-1}$ . The curves plotted over the data (red) are Gaussian fits. The red line indicates the mean of the distribution in log space and the error bars correspond to one standard deviation away from the mean in log space. The distribution of the Fe/O ratio for the boundary wind (panel (C)) is nearly identical to that of the fast wind (panel (B)) and distinctly different than the slow wind (panel (A)).

the differential streaming of heavy ions in the solar wind, as indicated by the difference between the alpha and proton speeds and the difference between the  $\text{O}^{6+}$  and the proton speed, as a function of solar wind velocity. This differential velocity has been theorized to be a result of wave–particle interaction (Isenberg & Hollweg 1983). As the solar wind is accelerated the heavier ions are accelerated preferentially up to an Alfvén speed faster than the protons (Marsch et al. 1982a). In these panels we can see that there is an average of a  $20 \text{ km s}^{-1}$  velocity difference between protons and alphas (panel (A)) in the fast solar wind (highlighted in blue). This same velocity difference is seen between  $\text{O}^{6+}$  and protons (panel (C)). In the slow solar wind (highlighted in red), the differential velocity is much smaller, indicating that the governing process in this wind is different from fast, coronal-associated wind. The differential streaming of the boundary wind (highlighted in green) is nearly identical to that of the fast solar wind, consistent with the boundary wind and the fast wind both being heated and accelerated by the same process. Panel (B) in Figure 6 shows the  $\text{O}^{6+}$  to proton temperature ratio. This panel shows that for the fast solar wind (highlighted in blue) the temperature of the wind is near mass proportional, with the  $\text{O}^{6+}$  kinetic temperature being 16 times that of the proton kinetic temperature (the red dotted line indicates mass proportional temperature ratio). At speeds larger than  $500 \text{ km s}^{-1}$  the solar wind temperature ratio is nearly mass proportional, while below  $500 \text{ km s}^{-1}$  the ratio drops toward equal temperature. This change in the temperature

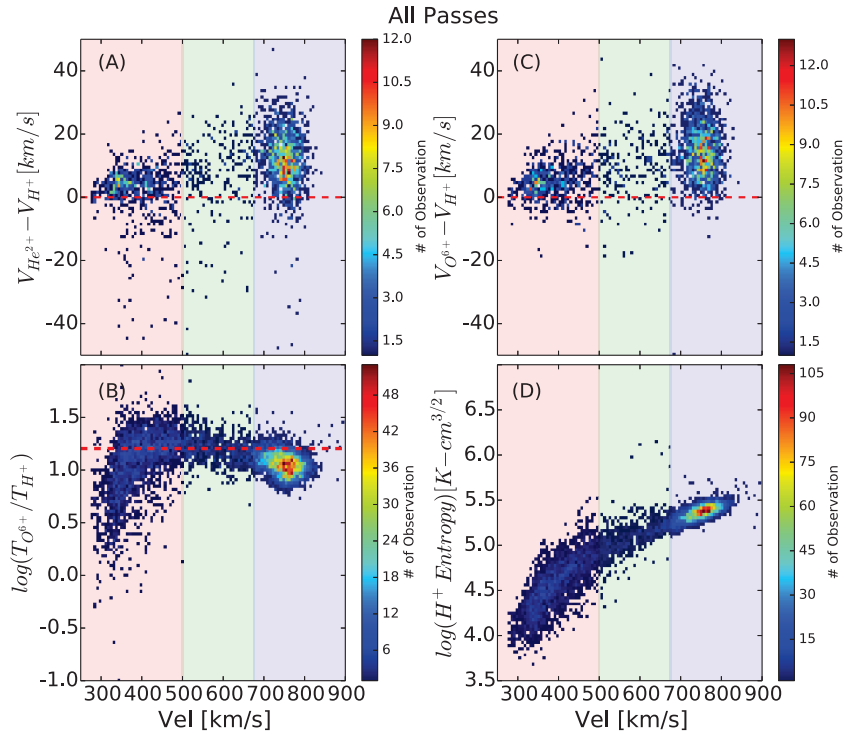


**Figure 6.** Kinetic properties for all of the Ulysses fast-latitude scans. Panel (A) shows the proton to alpha velocity difference. Panel (C) shows the  $O^{6+}$  to proton velocity difference. Both panels (A) and (C) filter the data to only include measurements that were taken over 66% of the time within  $30^\circ$  of the magnetic field being parallel to the radial direction. The red dotted line in panels (A) and (C) indicate no velocity difference. Panel (B) shows the temperature ratio between  $O^{6+}$  and protons. The red dotted line in panel (B) indicates a mass proportional temperature ratio. Panel (D) shows the proton entropy ( $T/n^{1/2}$ ). The highlighted colors in the background of the plots indicate the different types of solar wind: slow (red), boundary (green), and fast (blue). Panels (A) and (C) show the differential streaming between the protons and heavy ions are different in the slow wind ( $V < 500 \text{ km s}^{-1}$ ) than wind with velocity greater than  $500 \text{ km s}^{-1}$ . This same break in the properties of the wind at  $500 \text{ km s}^{-1}$  can also be seen in the temperature ratio (panel (B)) and entropy (panel (D)). This point also corresponds to the compositional distinction point seen in Figures 2–4.

ratio occurs at the same speed that the change in the elemental composition and differential velocity occur. The temperature ratio of the boundary wind (highlighted in green) is the same as the fast wind (highlighted in blue).

Panel (D) shows the specific entropy of the solar wind. The specific entropy of the solar wind is given by the formula  $T/n^{\gamma-1}$ , where  $T$  is the proton kinetic temperature and  $n$  is the density of the plasma. The polytropic index,  $\gamma$ , of the solar wind has previously been calculated by Totten et al. (1995) using the *Helios 1* data and found to have a value of  $\gamma = 1.46 \pm 0.04$ . This value is usually rounded to 1.5 (e.g., Burton et al. 1999; Pagel et al. 2004) leaving us with  $T/n^{1/2}$ . Typically the specific entropy of fast streams are higher than that of slow streams (Siscoe & Intriligator 1993). Numerous studies have looked into the correlation between the specific entropy of the solar wind and compositional ratios, specifically  $O^{7+}/O^{6+}$  (e.g., Burton et al. 1999; Crooker & McPherron 2012). Pagel et al. (2004) finds that there is a high correlation between the specific entropy and the  $O^{7+}/O^{6+}$  ratio outside of ICMEs and that the proton specific entropy is a reliable indicator of stream structure outside of solar maximum. In panel (D) of Figure 6 we use the entropy to study the differences in the solar wind types. Here we can see that there is a narrow range of observed specific entropy within the fast solar wind around  $250,000 \text{ K cm}^{3/2}$  and that this value follows an exponential dependence with solar wind velocity down to  $500 \text{ km s}^{-1}$ . Below  $500 \text{ km s}^{-1}$  the entropy deviates from this exponential dependence and steepens. The trend seen in this plot further exemplifies the similarities between the boundary wind and the fast solar wind and how they differ from the slow solar wind.

#### 4. DISCUSSION

The observed  $O^{7+}/O^{6+}$  and  $C^{6+}/C^{5+}$  ratios and the kinetic properties of the boundary solar wind indicate that there is a continuum of charge states that range from the slowest to the fastest speeds. The elemental composition data, on the other hand, highlights a distinct difference of origin in the wind at speeds below  $500 \text{ km s}^{-1}$  and the wind at speeds above  $500 \text{ km s}^{-1}$ . This distinction is further reinforced by the differences in the differential streaming, the entropy, and the ratios of the observed kinetic temperatures of oxygen and proton. Thus, during the observed time periods, there is a third type of wind—a boundary wind—between high-latitude fast (i.e.,  $v > 675 \text{ km s}^{-1}$ ) and slow (i.e.,  $v < 500 \text{ km s}^{-1}$ ) wind. We have shown that the fast wind and boundary wind have similar elemental composition, differential streaming, oxygen-to-proton-temperature ratio, and entropy slope versus speed. The similarities in these two types of wind lead us to believe that they originate from similar source regions and are heated and accelerated by the same mechanism near the Sun. Yet, the boundary wind is a subset of the fast solar wind that undergoes a significantly different expansion history than high-latitude fast wind, altering its ionic charge states and also observed solar wind speed and kinetic temperature. The slow solar wind, on the other hand, is distinguishable from both the boundary and high-latitude fast wind: Slow wind has little to no differential streaming, has a completely different oxygen to proton temperature profile and is compositionally distinct from the rest of the solar wind, indicating that it likely originates from a different source and is accelerated by a different mechanism.

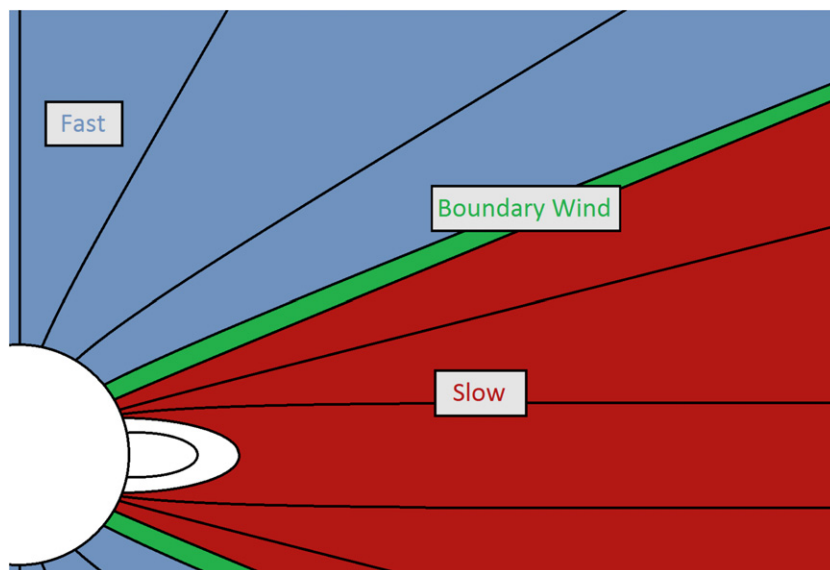


**Figure 7.** Diagram of the solar wind. The fast solar wind (blue) originates from the open magnetic field near the poles. The slow wind (red) originates from magnetic reconnection of closed coronal loops at the boundary of large scale streamers. The boundary wind (green) originates from open field lines near the boundary between coronal holes and streamers. It is to be noted that there is no sharp transition between the fast wind and the boundary wind, as the speed and charge-state composition of the former gradually approach those of the latter as the wind footpoint locations are closer to the coronal hole/streamer boundary.

One possible explanation for the increased charge-state ratios of the boundary wind over that of the fast wind is that the magnetic field near the boundary of coronal holes expands more than that of the magnetic field at the center. This expansion argument aligns with previous work done by flux-tube expansion (e.g., Wang et al. 2009, and references therein). This expansion leads to slower speed wind everywhere along the wind path. This slower speed results in more ionization to occur leading to increased charge states. The more expanded the flux tubes are, the greater the velocity decrease would be, resulting in a continuum of charge-state ionization from the barely expanded flux tubes near the center of coronal holes to the extremely expanded flux tubes at the edges. However, this process would not change the elemental composition of the plasma and would result in wind that has higher charge states and the same Fe/O ratio as the fast solar wind.

## 5. CONCLUSION

Several theories exist to explain solar wind heating and acceleration, including gradients in the Alfvén wave pressure, electric field acceleration due to electron charge separation and magnetic reconnection. In this paper we argue that it is possible for multiple methods to be active in the solar corona. The fast and boundary winds are two manifestations of the same type of wind originating from coronal holes and are heated and accelerated by the same process. However, the boundary wind originates closer to the boundary of the coronal hole, and therefore undergoes more expansion, leading to different wind speeds, electron temperatures, and densities at the foot points of coronal holes. As a consequence, this wind is compositionally very similar to the fast wind but has a lower velocity and increased ionization of heavy ions.

A more complete picture of the solar wind can be made using these results. In order to relate these findings to earlier work, Figure 7 shows a simplified picture of the Sun and the solar wind streaming from it. In this picture there exists three types of wind: slow, fast, and boundary wind. The slow wind (red) corresponds to the wind with speed lower than  $500 \text{ km s}^{-1}$ ,

likely produced by magnetic reconnection of closed and open field lines at the boundary between coronal holes and closed field regions. This interpretation of the slow wind is consistent qualitatively with Fisk (2003) and Antiochos et al. (2011). This wind originates from regions with high electron temperature and density resulting in more ionization of heavy ions. The fast solar wind (blue) originates from open magnetic field lines near the poles. This wind has lower charge states and ionization, higher speeds, and nearly photospheric elemental composition values. Finally we have the boundary wind (green) that originates from the edge of coronal holes; it is important to note that there is not a sharp divide between the fast and the boundary winds, as the speed and charge states of the former slowly and gradually change into those of the latter. This wind has an elemental composition identical to the fast solar wind but has decreased velocity and increased ionization, leading to a continuum of velocity and charge states between the fast and slow solar wind.

This work has been supported in part by grants from Living with a Star, NNX10AQ61G. T.H.Z. acknowledges the hospitality of the International Space Science Institute and helpful discussions with Dr. R. von Steiger. E.L. and S.T.L. acknowledge support from NASA grant NNX13AG22G.

## REFERENCES

- Antiochos, S. K., Mikić, Z., Titov, V. S., Lionello, R., & Linker, J. A. 2011, *ApJ*, **731**, 112
- Asplund, M., Grevesse, N., Sauval, A. J., & Scott, P. 2009, *ARA&A*, **47**, 481
- Balogh, A., Beek, T. J., Forsyth, R. J., et al. 1992, *A&AS*, **92**, 221
- Bame, S. J., McComas, D. J., Barraclough, B. L., et al. 1992, *A&AS*, **92**, 237
- Belcher, J. W., & Davis, L. J. 1971, *JGR*, **76**, 3534
- Burton, M. E., Neugebauer, M., Crooker, N. U., von Steiger, R., & Smith, E. J. 1999, *JGR*, **104**, 9925
- Cranmer, S. R., van Ballegoijen, A. A., & Edgar, R. J. 2007, *ApJS*, **171**, 520
- Crooker, N. U., Gosling, J. T., & Kahler, S. W. 2002, *JGRA*, **107**, 1028
- Crooker, N. U., & McPherron, R. L. 2012, *JGR*, **117**, A09104
- Ebert, R. W., McComas, D. J., Elliott, H. A., Forsyth, R. J., & Gosling, J. T. 2009, *JGR*, **114**, A01109
- Feldman, U. 1992, *PhysS*, **46**, 202
- Feldman, U., & Laming, J. M. 2000, *PhysS*, **61**, 222

- Feldman, U., Landi, E., & Schwadron, N. A. 2005, *JGRA*, **110**, 7109
- Fisk, L. A. 2003, *JGRA*, **108**, 1157
- Geiss, J., Gloeckler, G., & von Steiger, R. 1995, *SSRv*, **72**, 49
- Gloeckler, G., Geiss, J., Balsiger, H., et al. 1992, *A&AS*, **92**, 267
- Gloeckler, G., Zurbuchen, T. H., & Geiss, J. 2003, *JGRA*, **108**, 1158
- Gosling, J. T. 1997, in AIP Conf. Proc. 385, *Robotic Exploration Close to the Sun: Scientific Basis*, ed. S. R. Habbal (Melville, NY: AIP), 17
- Grevesse, N., & Sauval, A. J. 1998, in *Solar Composition and Its Evolution—From Core to Corona*, ed. C. Fröhlich, M. C. E. Huber, S. K. Solanki, & R. von Steiger (Dordrecht: Kluwer), 161
- Hollweg, J. V. 1986, *JGR*, **91**, 4111
- Isenberg, P. A., & Hollweg, J. V. 1983, *JGRA*, **88**, 3923
- Lemaire, J., & Scherer, M. 1971, *JGR*, **76**, 7479
- Lemaire, J., & Scherer, M. 1973, *RvGSP*, **11**, 427
- Marsch, E. 1991, in *Physics of the Inner Heliosphere, Vol. II, Particles, Waves and Turbulence*, ed. R. Schwenn & E. Marsch (Berlin: Springer), 45
- Marsch, E., Mühlhäuser, K.-H., Rosenbauer, H., et al. 1982a, *JGR*, **87**, 35
- Marsch, E., Mühlhäuser, K.-H., Schwenn, R., et al. 1982b, *JGR*, **87**, 52
- Pagel, A. C., Crooker, N. U., Zurbuchen, T. H., & Gosling, J. T. 2004, *JGR*, **109**, A01113
- Parker, E. N. 2010, in AIP Conf. Proc. 1216, *Twelfth International Solar Wind Conference*, ed. M. Maksimovic et al. (New York, NY: AIP), 3
- Schwenn, R. 1990, in *Physics of the Inner Heliosphere, Vol. I, Large-scale Phenomena*, ed. R. Schwenn & E. Marsch (Berlin: Springer), 99
- Siscoe, G. L., & Intriligator, D. 1993, *GeoRL*, **20**, 2267
- Totten, T. L., Freeman, J. W., & Arya, S. 1995, *JGR*, **100**, 13
- van der Holst, B., Sokolov, I. V., Meng, X., et al. 2014, *ApJ*, **782**, 81
- von Steiger, R., Schwadron, N. A., Fisk, L. A., et al. 2000, *JGR*, **105**, 27217
- von Steiger, R., & Zurbuchen, T. H. 2006, *GeoRL*, **33**, L09103
- Wang, Y.-M., Ko, Y.-K., & Grappin, R. 2009, *ApJ*, **691**, 760
- Widing, K. G., & Feldman, U. 2001, *ApJ*, **555**, 426
- Zurbuchen, T. H. 2007, *ARA&A*, **45**, 297
- Zurbuchen, T. H., Fisk, L. A., Gloeckler, G., & von Steiger, R. 2002, *GeoRL*, **29**, 1352
- Zurbuchen, T. H., & von Steiger, R. 2006, in *Proceedings of the Conference, SOHO-17. 10 Years of SOHO and Beyond*, ed. H. Lacoste & L. Ouwehand, (ESA SP-617; Noordwijk, ESA), 7.1